ARTICLE   OPEN

Tensorial stress–strain fields and large elastoplasticity as well as friction in diamond anvil cell up to 400 GPa

Valery I. Levitas [ID][1,2]*, Mehdi Kamrani[3] and Biao Feng[4]

Various phenomena (fracture, phase transformations, and chemical reactions) studied under extreme pressures in diamond anvil cell are strongly affected by fields of all components of stress and plastic strain tensors. However, they could not be measured. Here, we suggest a coupled experimental−theoretical−computational approach that allowed us (using published experimental data) to refine, calibrate, and verify models for elastoplastic behavior and contact friction for tungsten (W) and diamond up to 400 GPa and reconstruct fields of all components of stress and large plastic strain tensors in W and diamond. Despite the generally accepted strain-induced anisotropy, strain hardening, and path-dependent plasticity, here we showed that W after large plastic strains behaves as isotropic and perfectly plastic with path-independent surface of perfect plasticity. Moreover, scale-independence of elastoplastic properties is found even for such large field gradients. Obtained results open opportunities for quantitative extreme stress science and reaching record high pressures.

INTRODUCTION

In static high-pressure research, megabar pressures are generated by compression of a thin sample by two diamonds in diamond anvil cells (DAC)[1–4]; see Fig. 1. This process is accompanied by large plastic deformation of a sample and large elastic deformation of the diamond.[5,6] Various problems, such as the study of physical, chemical, geological, and mechanical phenomena and synthesis of new phases in a sample, as well as the increasing range of achievable pressures,[1–23] are related to knowledge of the fields of all components of the stress, elastic, and plastic strain tensors in DAC. While most measurements and discussions are related to pressure only, it is evident that elastic deformation and fracture of diamond and plastic flow of a sample and gasket depend on all components of the stress tensor. Contact friction between diamond and sample/gasket plays a key role in generating high pressure without fracture of the diamond; friction is a shear stress that depends on the stress normal to the contact surface. It is also well-known that phase transformations and chemical reactions in solids depend not only on pressure, but also on the deviatoric stresses and plastic strains.[12,14–16,20–23] All of these fields are extremely complex and heterogeneous, e.g. with normal stresses varying by megabar over 20 μm.[6,7]

Measurement of the radial pressure distribution at the sample-diamond boundary was based on the ruby fluorescence method, which worked up to 185 GPa.[4] For higher pressure, radial pressure distribution averaged over the sample thickness is determined using X-ray diffraction in a sample.[6,7] The radial thickness profile, which characterizes both elastic deformation of an anvil and elastoplastic deformation of a sample/gasket, was measured utilizing in situ high-pressure X-ray absorption.[6,7] Measurement of the deviatoric stress was limited to the difference between axial stresses σ_{zz} and radial stresses σ_{rr} averaged over the entire sample.[8,9,17–19] Plastic deformation fields in the sample compressed in DAC and contact friction stresses were not measured at

all. Thus, despite significant progress, it is unlikely that all tensorial fields in DAC will be measured. Theoretical approaches and finite element method (FEM) simulations[23–29] of the DAC are based on relatively simple models with linear pressure dependence of the yield strength and simplified contact friction conditions. The most sophisticated model and the best numerical reproduction of the experimental pressure distribution in ref.[5] was obtained in ref.[27] for compression of rhenium up to 285 GPa. However, in that study the plastic sliding along the contact surface and also the dependence of the friction coefficient on the normal contact pressure were ignored. Also, good correspondence was obtained for one pressure distribution only; for two smaller pressure levels, significant deviation from the experiment existed, i.e. the model is not adequate. To obtain such a description of the experiment, the third-order elastic constants of diamond were modified. Besides, since experimental thickness profiles of the sample were not available, reproducing the pressure distributions was aimed only. Thus, while essential improvement in reproducing pressure distribution in comparison with the previous works[26,27] was achieved, obtained mechanical properties cannot be considered as verified, and corresponding stress and plastic strain tensor fields may contain significant inaccuracies.

We suggest the following coupled experimental−theoretical−computational approach for determination of all stress and plastic strain tensorial fields, elastoplastic properties, and contact friction rules. All fields that can be measured should be measured. Physics-based models for elastoplastic behavior and contact friction should be iteratively developed and refined, and all material properties should be calibrated by fitting to some experimental fields and verified by comparison with other experimental fields. With these properties, simulations provide all fields, including components of the stress and plastic strain tensors, friction stress, etc., i.e., those which cannot be directly measured. To obtain the first results from this method, we will use

[1]Departments of Aerospace Engineering and Mechanical Engineering, Iowa State University, Ames, IA 50011, USA. [2]Division of Materials Science and Engineering, Ames Laboratory, Ames, IA 50011, USA. [3]Department of Aerospace Engineering, Iowa State University, Ames, IA 50011, USA. [4]Los Alamos National Laboratory, Los Alamos, NM 87545, USA. *email: vlevitas@iastate.edu
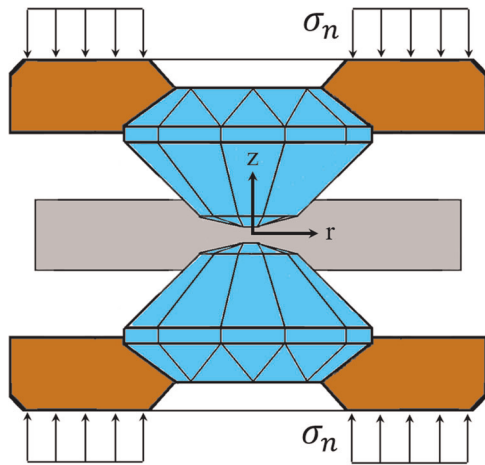
V.I. Levitas et al.

Fig. 1 DAC scheme: Two diamond anvils compress a sample

the most advanced experimental data on compression of W in DAC up to 400 GPa[6] and slightly generalize our models for large elastoplastic deformations and contact friction from.[24,27]

RESULTS AND DISCUSSION
Model

A complete system of equations for fourth-order elasticity of diamond, large elastoplastic deformation of W, combined Coulomb and plastic friction, geometry of DAC, formulation of axisymmetric problem in cylindrical coordinates $rz\theta$, and nonlinear elastic properties are presented in the Methods section. It is known that the yield surface in the six-dimensional space of components of the stress tensor evolves during plastic deformation (Fig. 13), exhibiting strain hardening; this evolution depends on the entire history of plastic strain, and material acquired deformation-induced anisotropy.[24,30] It was suggested in ref. [24] as the postulate of the perfect plasticity that, above some level of accumulated plastic strain $q > m$ (q is defined in Eq. (11)) and for a deformation path without sharp changes in directions (monotonous deformation), the initially isotropic polycrystalline materials are deformed as perfectly plastic and isotropic with a strain-history-independent surface of the perfect plasticity (Fig. 13). This statement means that (1) the strain hardening is saturated, and that (2) strain-induced anisotropy and path dependence do not exhibit themselves at monotonous loading. Some qualitative arguments in favor of the postulate of the perfect plasticity have been analyzed,[24] but quantitative proof was not given for any material. Here, we incorporated this postulate into our model and will prove that such a model describes well experimental data. Our model is based on the linear pressure dependence of the yield strength in compression $\sigma_y = \sigma_{0y} + ap$ with two material parameters, with no plastic strain or plastic strain path dependence. Another hypothesis that will be proven is that despite the μm-sized sample thickness and huge stress and plastic strain gradients, i.e. conditions that require utilization of scale-dependent and the gradient plasticity,[31–33] much simpler local plasticity provides adequate description of experiments.

Contact friction stress is determined either by the Coulomb law $\tau_f = \tau_f^c = \mu(\sigma_c)\sigma_c$, where σ_c is the normal contact stress and μ is the friction coefficient, or by the yield strength in shear $\tau_f = \tau_y(p) = \sigma_y(p)/\sqrt{3}$ (plastic friction), whichever is smaller. Sticking occurs if the contact shear stress is smaller than these critical values τ_f. All of our assumptions for the yield strength (independence of plastic strain and its path) are also involved in the assumption for plastic friction. The friction coefficient is usually taken as a constant[27] because no experimental data under high

pressure are available. We assume $\mu = \mu_0 + c\sigma_c$ with two material parameters.

In addition, some of the third-order elastic constants of W and fourth-order elastic constants of diamond, which are not well defined from the literature, are refined by comparison with DAC pressure and sample thickness distributions.

To summarize, in comparison with ref. [27], current model includes fourth-order elasticity of diamond, combined Coulomb and plastic contact sliding, and linear pressure dependence of the Coulomb friction coefficient. Moreover, all unknown material parameters are calibrated using one set of experimental data and verified using another experimental set.

Results

All four material parameters in the pressure dependence of the yield strength and friction coefficient were calibrated by minimizing the error between experimental and FEM results for pressure distributions for *two curves* with maximum pressures $p_{max} = 170$ and 240 GPa (Fig. 2a). This led to

$$\sigma_y = 1.8 + 0.1p; \quad p \leq 225\,\text{GPa} \quad \mu = 0.05 + 0.001\sigma_c; \quad \sigma_c \leq 37\,\text{GPa}.$$
(1)

Unexpected strong limitations on pressure and contact stress appear because we found in FEM solutions that Coulomb sliding and plastic flow do not occur for $\sigma_c > 37$ GPa and $p > 225$ GPa, respectively. With properties in Eq. (1), good correspondence is obtained for *two other* pressure distributions with $p_{max} = 300$ and 400 GPa, with a maximum difference not exceeding 10% (Fig. 2a). In addition, the profile of the sample after very large compression and deformed anvil surface were reproduced for all *four* pressures, with a maximum discrepancy smaller than 1 μm (Fig. 2b, c). Both discrepancies are within error for an experiment under such extreme conditions. As seen in Fig. 2, properties in Eq. (1) result in having good agreement with experimental pressure distribution not only at large pressures, but also at low pressures where the error in the experimental results is assumed to be the least. The achieved good agreement at lower pressures is missing in ref. [27]. Besides, thickness profiles are properly reproduced. The curves in Fig. 2 are nontrivial, and coincidence demonstrates strong verification of the entire model and the specific material properties from Eq. (1). It also proves the *validity of the postulate of the perfect plasticity* for W, which was directly incorporated in our model, and *sufficiency of the local elastoplastic model* even at micron scale and with huge stress and plastic strain gradients. In summary, *elastoplasticity and, consequently, plastic friction under such large strain and pressure is plastic strain-, plastic strain path-, and scale-independent*, which drastically simplifies theory and measurements.

In addition, the higher-order elastic constants of W and diamond, which have large scatter in literature (see the Methods section), have been also refined/identified. Thus, we found the third-order constants for W, $m = -1081$ and $n = -1164$ GPa, to obtain a slightly better fit to the experimental pressure distribution curves for three lowest pressure. The fourth-order elastic constant of diamond, $C_{1112} = 31,214$, $C_{1122} = 20,044$, and $C_{1266} = 819$ GPa, were found from the best fit to the sample profile under highest pressure only under constraint that they satisfy the known equation of state of diamond; see the Methods section.

The suggested method has high throughput features, which allows to determine ten material parameters using three pressure and one sample thickness distributions.

Known[5] pressure dependence of the yield strength for W has huge scatter (Fig. 3), which is related to numerous assumptions for the determination of $\sigma_y(p)$ and to attribution of the dependence of σ_y on plastic strain to the pressure dependency. In our curve, the effect of plastic strain is excluded and the correctness of Eq. (1) is confirmed by numerous data in Fig. 2.
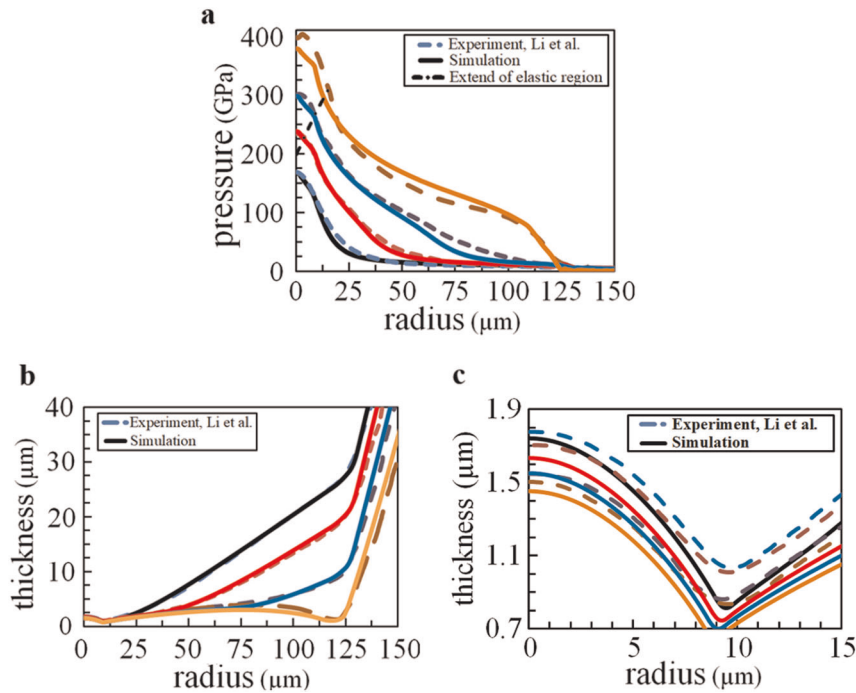
Fig. 2 Calibration and verification of the model for DAC. **a** Radial distributions of pressure. **b** Corresponding sample thickness (anvil profile) in experiment[6] (dash lines) and FEM simulations (solid lines). **c** Zoomed sample thickness profile from (**b**) at the central region of the sample. Dash-dot line in (**a**) shows the radius of the central region where the sample deforms elastically after initial plastic flow. Material functions in Eq. (1) were determined from the best fit to two low-pressure curves in (**a**). Good correspondence with experiments for two high-pressure curves in (**a**) and all four thickness curves after very large compressions in (**b**) and (**c**) provides strong and nontrivial verification of the model
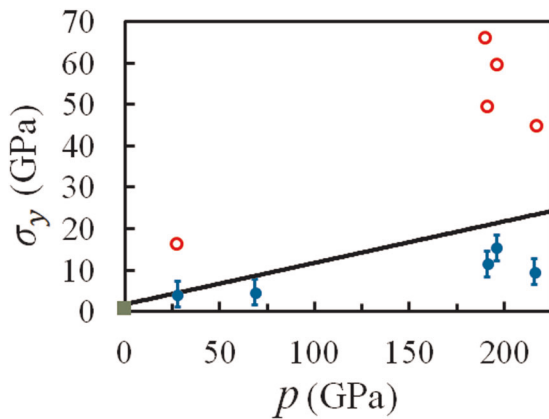

Fig. 3 Pressure dependence of the yield strength after large plastic deformation. Solid line is based on Eq. (1) obtained using experimental data from ref. [6]; symbols are from ref. [5]. Large scatter-in data from ref. [5] is related to multiple assumptions for the determination of the yield strength and to attribution of the dependence of σ_y on plastic strain to the pressure dependency

After proving its validity, the model is used for computational reconstruction of all fields of interest. Distribution of shear friction stress and normalized radial sample velocity along the diamond-sample contact surface at different pressures is shown in Fig. 4a, b. Such a complex profile of shear stresses and their evolution are nontrivial and counterintuitive. In particular, shear stress in the sticking zone makes several oscillations in a central cup region, and the sticking zone grows with increasing compression. The plastic friction zone is surprisingly narrow, which does not allow use of the traditional method for determination of $\tau_y(p)$ based on a pressure gradient.[7,13,24] The maximum yield strength in shear and corresponding p in the plastic sliding zone *reduces* from

5.85 GPa and 77.2 GPa for $p_{max} = 164$ GPa to 3.7 GPa and 44 GPa for $p_{max} = 380$ GPa. The maximum shear stress in the Coulomb sliding zone is 3.21 GPa, corresponding to $\sigma_c = 37$ GPa; for $p_{max} = 380$ GPa, it is 2 GPa, corresponding to $\sigma_c = 26.2$ GPa. An important conclusion is that, due to significant increase in the sticking zone, an increase in p_{max} does not lead to an increase in the maximum range of σ_c and friction stress, either for Coulomb or plastic friction. The only way to increase these ranges is to use torsion under a fixed force in rotational DAC,[12,15,22,34–36] for which FEM simulations[29,37] show that the sticking zone is localized near the center.

The sample particles' radial velocity along the diamond-sample contact surface (Fig. 4b) is directed toward the center in the sticking zone for any pressure, and is equal, by the definition of sticking, to the velocity of the diamond contact particles. Outside the sticking zone, sample particles move away from the center, achieving maximum velocity at the edge of the culet. The maximum velocity increases to $p_{max} = 231$ GPa, then reduces due to the increasing sticking zone.

All relevant fields in the central part of the W sample at maximum pressure of 300 GPa are presented in Fig. 5 on a quarter of the sample, due to the symmetries. While axial stress σ_{zz} is independent of the z coordinate, radial stress σ_{rr} visibly depends on z and pressure p is, by definition, in between.

All components of plastic strain and q are very heterogeneous and reach very large values. Plastic shear strain ε_p^{rz} (defined in Eq. (6)) changes sign three times in the central zone. Accumulated plastic strain q reaches its maximum value at the contact surface, especially where the thickness is smallest. Note that, for uniaxial compression/tension, q reduces to the logarithmic strain, and maximum $q = 5.77$ in Fig. 5c corresponds to the ratio of the initial-to-final length of $exp(5.77) = 321$. With increasing radius, q increases further. Material rotation in Fig. 5c, which leads to the development of texture, is also very large, with a maximum of 46.8° in this region. Thus, if strain-induced anisotropy would be
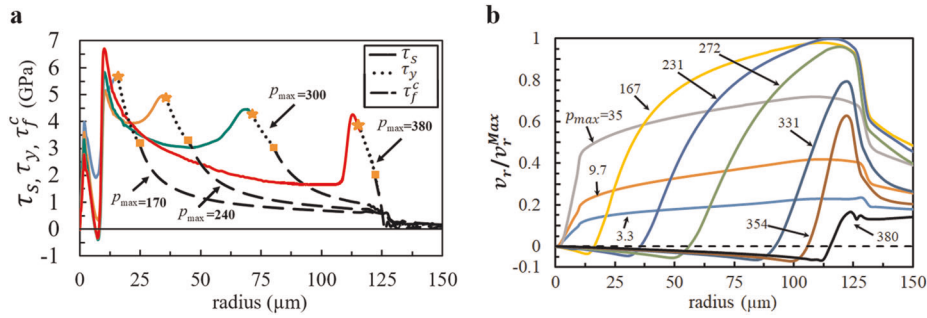
Fig. 4 Contact friction and velocities. **a** Distribution of shear friction stress and **b** normalized sample radial velocity along the diamond-sample contact surface at various pressures. In (**a**), along each given curve, with reducing radius, i.e. from low to high pressure, the dashed portion corresponds to the Coulomb friction τ_f^c until shear stress reaches the yield strength in shear $\tau_y(p)$ (designated by squares). The dotted line between squares and stars corresponds to the plastic sliding with $\tau_c = \tau_y(p)$. The solid line τ_s between stars and center of the sample corresponds to sticking between anvil and sample. Numbers near curves in (**a**) and (**b**) designate maximum pressure. Velocity is normalized by maximum velocity at $p_{max} = 231$ GPa
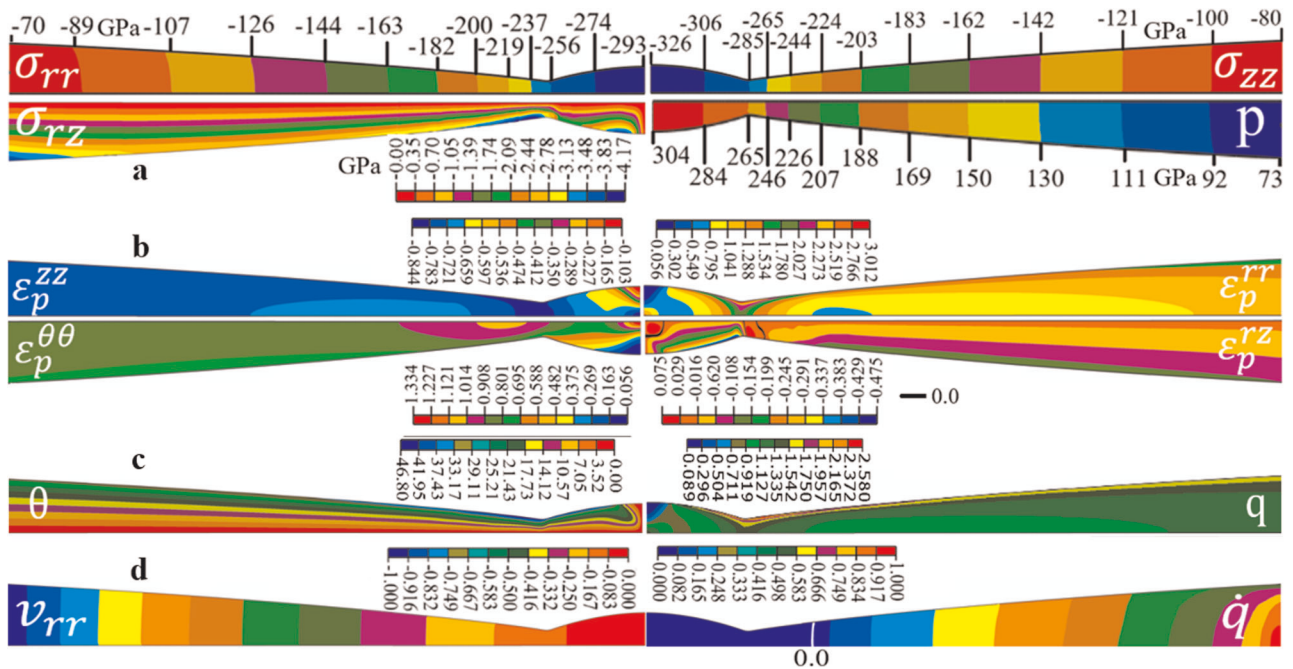

Fig. 5 Stress, plastic strain, and rate fields for $p_{max} = 300$ GPa. **a** Fields of components of the stress tensor and pressure p, **b** plastic strain tensor $\boldsymbol{\varepsilon}_p$ (defined in Eq. (6)), **c** accumulated plastic strain q, and particles' rotation angle θ, and **d** normalized radial velocity v_{rr} and $\dot{q}$ in the central part of a sample for $r < 60$ μm. See Methods section for definition of parameters. Scale of the thickness vs. length is multiplied by four here and in all similar figures below

present, isotropic flow theory would not describe experiments. The rotation angle, similar to shear stress σ_{rz}, is zero at the symmetry axis and plane and increases with increasing r and z. Radial velocity (Fig. 5d) at such a pressure is directed toward the center in the entire region. It is independent of z and its magnitude increases with r. The rate of accumulated plastic strain $\dot{q}$ also increases with r, with zero region to the left of the white line in Fig. 5d, where plastic flow stops and the material deforms elastically. Evolution of the elastic zone with increasing pressure is shown in Fig. 2a. It appears at $p_{max} = 200$ GPa and increases with increasing pressure due to cupping of diamond.

Similar fields for three other maximum pressures, which we used for calibration and verification of the model, are given in Figs 6–8. For lower pressures, we present components of the stress tensor and pressure only in Fig. 9.

In the maximum pressure range from 170 to 380 GPa, axial stress σ_{zz} is independent of the z coordinate, radial stress σ_{rr} shows

visible dependence on z and pressure p is in between. Degree of heterogeneity of σ_{rr} and p increases with reducing maximum pressure because of more intense plastic flow. With further maximum pressure reduction, σ_{zz} acquires some heterogeneity at the center of the sample and around corner point between beveled and initially flat central part. The heterogeneity of σ_{zz} is quite pronounced in the entire central region for maximum pressure in the range of 1 to 10 GPa, while below the beveled part of the anvil σ_{zz} and even pressure is quite homogeneous along z coordinate. Shear stresses have generally similar patterns for any maximum pressure, governed by zero stress at the symmetry plane and axis and increasing shear stress with increasing z and r. In the pressure range from 1 to 10 GPa, maximum shear stress is smaller than the yield strength in shear and either sticking or Coulomb friction are involved. Due to increase in the yield strength, maximum shear stress increases when maximum pressure growth from 10 to 100 GPa, then it reduces due to the
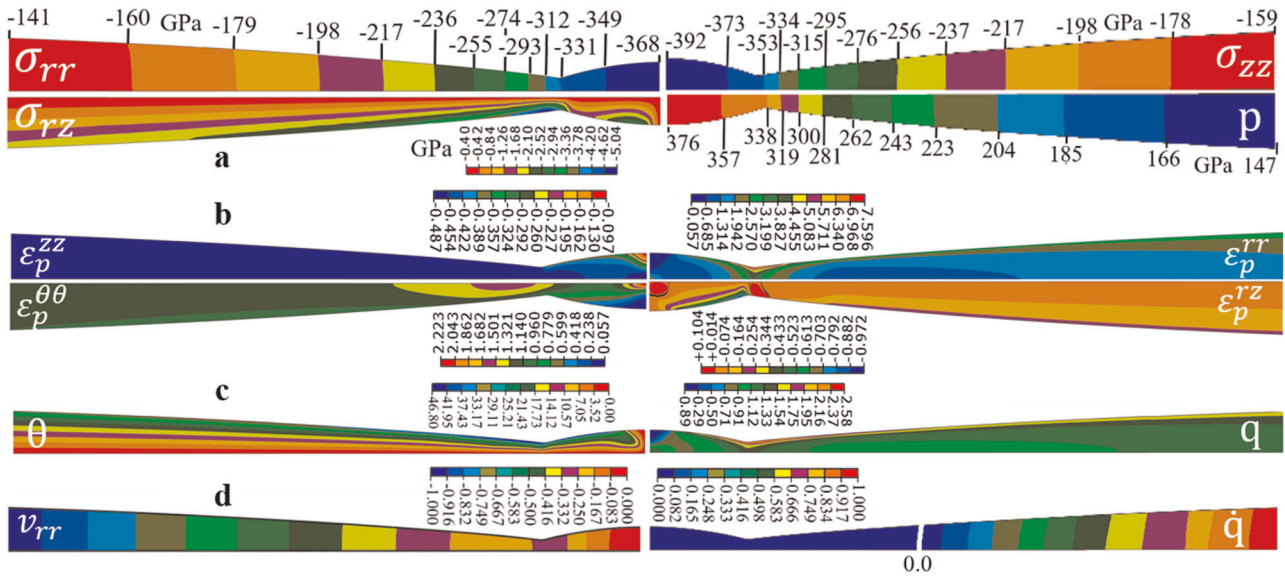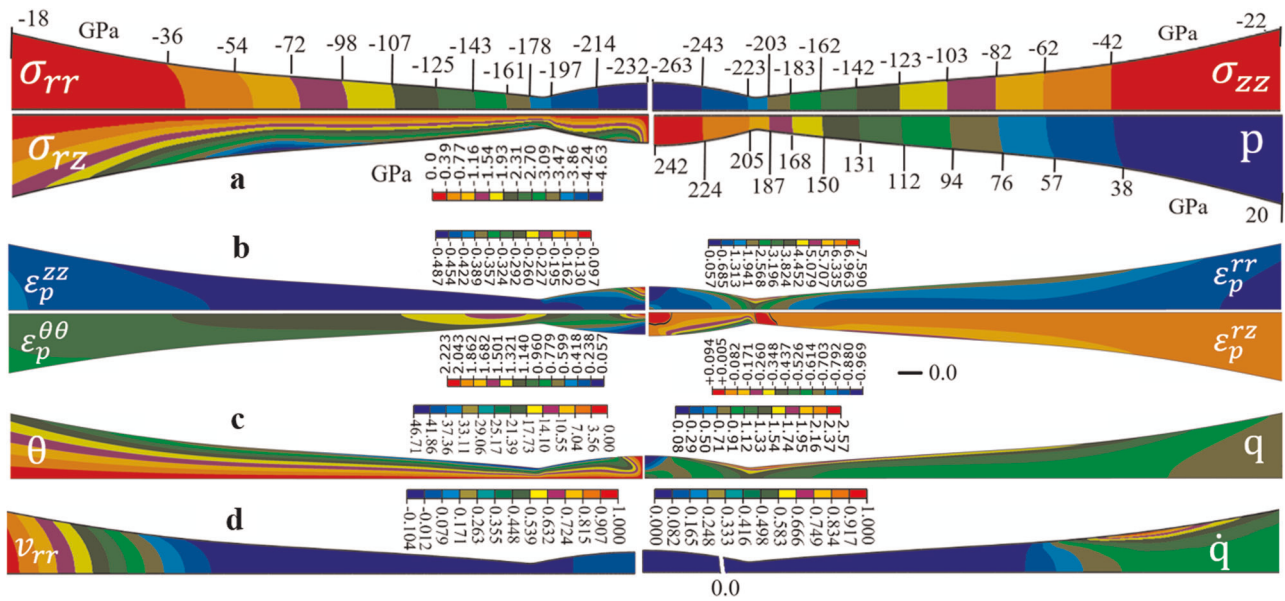
Fig. 6 Stress, plastic strain, and rate fields for $p_{max} = 376$ GPa. **a** Fields of components of the stress tensor and pressure p, **b** plastic strain tensor ε_p, **c** accumulated plastic strain q, and particles' rotation angle θ, and **d** normalized radial velocity v_{rr} and $\dot{q}$ in the central part of a sample for $r < 60$ μm

Fig. 7 Stress, plastic strain, and rate fields for $p_{max} = 240$ GPa. **a** Fields of components of the stress tensor and pressure p, **b** plastic strain tensor ε_p, **c** accumulated plastic strain q, and particles' rotation angle θ, and **d** normalized radial velocity v_{rr} and $\dot{q}$ in the central part of a sample for $r < 60$ μm

effect of significant cupping. Some cupping is first visible at $p_{max} = 50$ GPa and is quite pronounced at $p_{max} = 100$ GPa.

Fields of plastic strain tensor ε_p, accumulated plastic strain q, and particles' rotation angle θ, as well as normalized radial velocity v_{rr} and $\dot{q}$ have similar patterns for all maximum pressures in the range from 170 to 380 GPa. However, region with elastic deformations without plasticity at the center of the sample is getting visible at $p_{max} = 240$ GPa and increases with further loading.

All stress fields in the central part of the diamond for $p_{max} = 300$ GPa are presented in Fig. 10. All normal stresses have their maximum at the center of the culet, with $\sigma_{zz}^{max} = -321$ GPa and $\sigma_{rr}^{max} = \sigma_{\theta\theta}^{max} = -260$ GPa, i.e. nonhydrostaticity is very high. Maximum shear stress $\sigma_{rz}^{max} = 37.5$ GPa is located away from the culet. This value is significantly smaller than the theoretical shear

strength of 96.6 GPa at zero pressure, which grows with pressure.[36] It is important that the regions in which maximum normal and shear stresses occur do not overlap.

The obtained fields of all components of the stress tensor are the basis for the development of criteria for fracture of diamond. To illustrate the concept, consider experimentally observed fracture due to compression stress $\sigma_{[110]}$ along the [110] direction. Theoretical strength for compression along the [110] direction obtained in refs [38,39] using ab initio simulations can be approximated as $\sigma_{th}^{[110]} = -471 + 1.64\sigma_{bi}$ (GPa), where σ_{bi} is the averaged biaxial normal stress in planes orthogonal to (110); in our case $\sigma_{bi} = 0.5\left[\sigma^{[\bar{1}10]} + \sigma_{\theta\theta}\right]$, where $\sigma^{[\bar{1}10]}$ is normal stress along the $[\bar{1}10]$. The equivalent normalized stress in direction [110], plotted in Fig. 10, is then $\sigma_{eq}^{[110]} = \sigma^{[110]}/\sigma_{th}^{[110]}$, and fracture occurs at
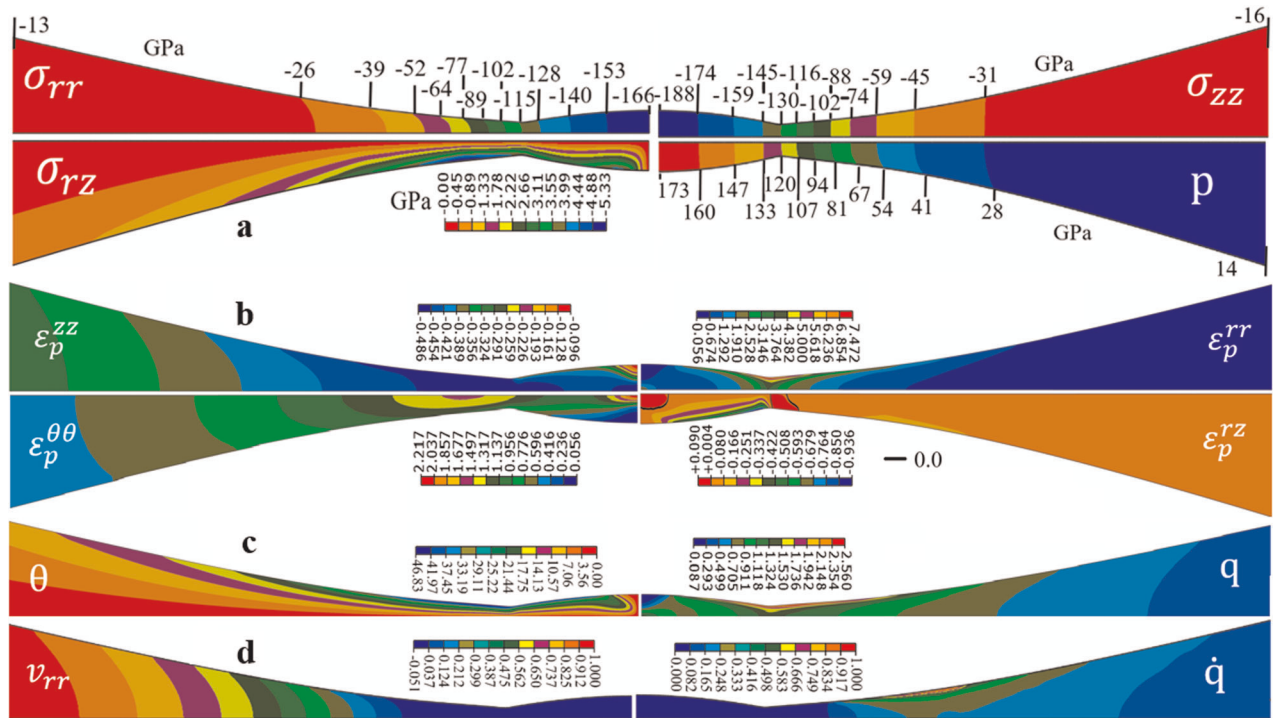
Fig. 8 Stress, plastic strain, and rate fields for $p_{max} = 170$ GPa. **a** Fields of components of the stress tensor and pressure p, **b** plastic strain tensor ε_p, **c** accumulated plastic strain q, and particles' rotation angle θ, and **d** normalized radial velocity v_{rr} and $\dot{q}$ in the central part of a sample for $r < 60\,\mu m$

$\sigma_{eq}^{[110]} = 1$. Since maximum $\sigma_{eq}^{[110]} = 0.32$, there is still a significant safety factor for ideal diamond along the [110] direction. For complete fracture analysis, similar distributions should be obtained for other possible fracture planes and shear stresses along these planes should be also taken into account. This is the key problem, the solution of which will allow optimization of the design of anvils and loading conditions for a perfect crystal, which will provide the upper bound of achievable pressure (stresses), provided that plastic deformation in diamond does not occur. Introducing defects into simulations will open the possibility of developing the fracture mechanics and plasticity of real diamond crystals under extreme stresses.

In summary, we suggested a novel coupled experimental −theoretical−computational approach that allowed us (using known experimental data from ref. [6]) to extract complete information about elastoplastic properties and friction rules, as well as all complex tensorial fields for materials compressed in a DAC under extreme pressure. In particular, we refined, calibrated, and verified models for elastoplastic behavior of a sample and contact friction for W up to 400 GPa and reconstruct fields of all components of stress and large plastic strain tensors in W and diamond. In addition to quantitative information on the pressure dependence of the yield strength and friction, as well as higher-order elastic constants, we justify some general unique properties of elastoplastic behavior under very large strains and pressures:

(a) Despite the generally accepted strain-induced anisotropy, strain hardening, and path-dependent plasticity, W after large plastic strains behaves isotropically and does not exhibit strain hardening and path dependence.
(b) Despite the μm-sized sample thickness and huge stress (5 GPa/μm) and plastic strain gradients, scale-independence of elastoplastic properties is found.

Both of these properties drastically simplify plasticity theory and measurements under extreme conditions.

Our finding for plasticity also implies important properties for plastic friction under such extreme loading: Plastic friction is plastic strain-, plastic strain path-, and scale-independent.

Complex and counterintuitive profile of contact shear stresses and their evolution are found. The plastic friction zone is surprisingly narrow, which does not allow use of the traditional method for determination of $\tau_y(p)$ based on a pressure gradient.[7,13,24] Despite the maximum pressure of 380 GPa, plasticity and plastic sliding occur below 225 GPa, and Coulomb friction takes place below 37 GPa only. Due to significant increase in the sticking zone, an increase in p_{max} above 240–300 GPa leads to decrease in the maximum range of pressure and contact stress σ_c at which plastic flow, Coulomb or plastic friction occur. The only way to increase these ranges for characterization of plastic flow and contact friction is to use torsion under a fixed force in rotational DAC,[12,15,22,34–36] for which FEM simulations[29,37] show that the sticking zone is localized near the center.

The field of all components of the stress tensor in diamond are the basis for the development of criteria for fracture of diamond. We illustrated the concept by considering fracture due to compression along one of the experimentally observed directions. This is an important step which after detailed study of fracture of anvil will allow optimization of the design of anvils and loading conditions for further increase in achievable pressure.

The developed experimental−theoretical−computational approach allows different realizations for different available experimental data. In particular, recently developed nanoscale sensing platform,[40] which integrates nitrogen-vacancy color centers directly into the culet of diamond anvils, allows experimental determination of distribution of all six components of the stress tensor in diamond along the flat culet, i.e., at the contact surface with the sample. This information allowed us to reconstruct nontrivial normal and shear contact stresses between diamond and gasket and fields of all components of stress tensor in the entire anvil. Since linear response is utilized, this method was applied up to 30 GPa.
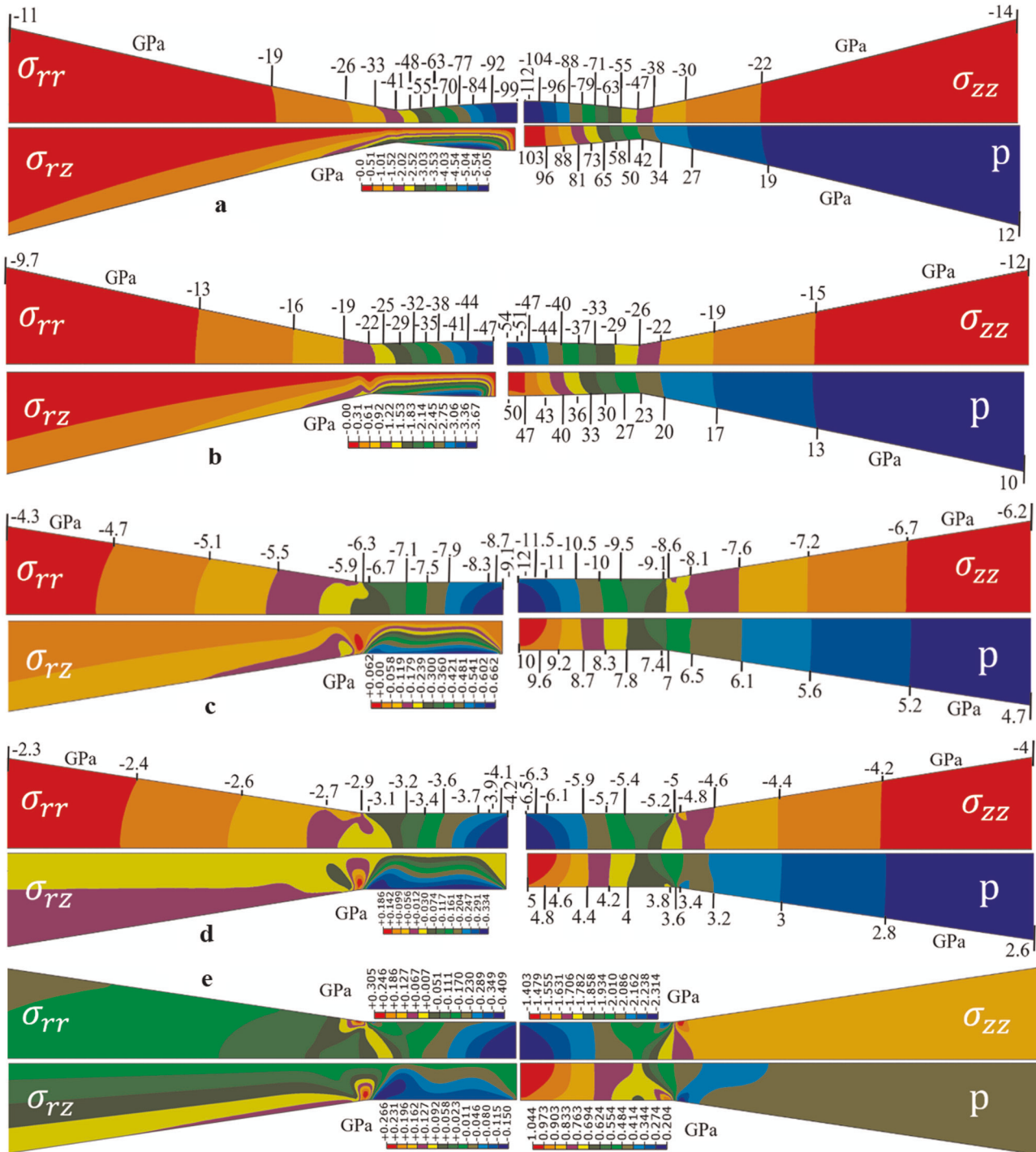
Fig. 9 Components of stress tensor and pressure for different maximum pressures. **a** $p_{max} = 100$ GPa, **b** $p_{max} = 50$ GPa, **c** $p_{max} = 10$ GPa, **d** $p_{max} = 5$ GPa, **e** $p_{max} = 1$ GPa, in the central part of a sample for $r < 60\ \mu m$

Note that W is used as a gasket material in DAC at megabar pressures, i.e. obtained results have also applied importance for study of various sample materials within W gasket. Knowledge of the distributions of all (generally 12) components of stress and plastic strain tensors in a sample will allow study of their (instead of pressure alone) effect on phase transformations, chemical reactions,[12,14–16,20–22,34–37] and various physical properties. In comparison with research under hydrostatic pressure, this will add up to 11 new dimensions to the parametric space for studying these processes, searching for new phases and materials,

drastically reducing the required pressure for synthesis of new and known materials with unique properties, and understanding processes in the deep interiors of the Earth and other planets. Obtained results will also enable calibration and verification of known and new methods for measurement of the components of stress tensors in anvils and samples.

METHODS
A complete system of equations for fourth-order elasticity of diamond, large elastoplastic deformation of W, and combined Coulomb and plastic
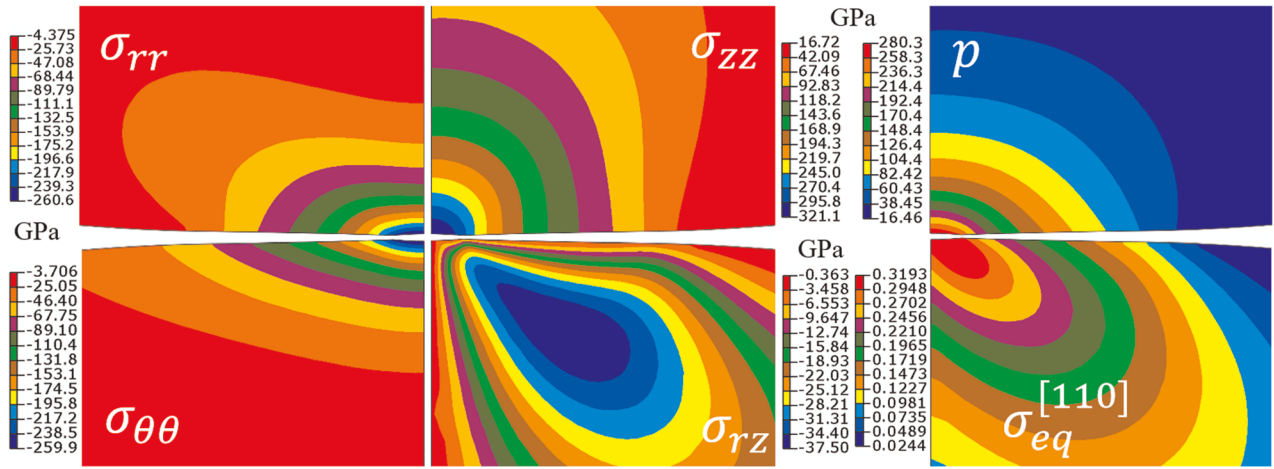
Fig. 10 Field of the components of the stress tensor, pressure, and equivalent stress $\sigma_{eq}^{[110]}$ near the tip of a diamond anvil for $r < 100$ and $z < 70\,\mu m$ for $p_{max} = 300\,GPa$
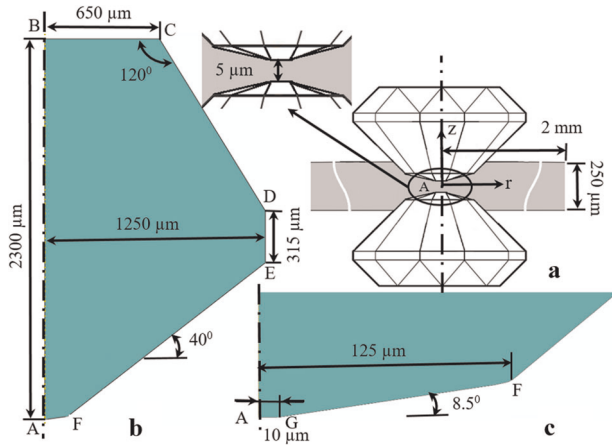

Fig. 11 a Mao-type DAC scheme and the geometric parameters of the sample in the initial undeformed state. **b** Geometric parameters of a quarter of the diamond anvil, and **c** the tip of the diamond anvil in the initial undeformed state

friction, as well as problem formulation are presented in this section. Finite element algorithm presented in ref. [27] was utilized for solution of all boundary-value problems.

Geometry and boundary conditions

Axisymmetric problem formulation is considered. Due to symmetry of the Mao-type DACs used in ref. [1], only the upper part of the DAC and sample will be used in simulations. Geometry of the sample and the anvil, as well as the boundary conditions, are shown in Fig. 11 and are as follows:

(1) A uniform vertical displacement is applied at the boundary between the top inclined surface of the anvil and Boehler-type seat (line CD). Distribution of stresses or displacements along this surface does not affect fields close to the diamond culet (line AG).

(2) At the symmetry axis $r = 0$ (line AB), shear stress σ_{rz} and horizontal displacements are zero. At the symmetry plane $z = 0$, shear stress σ_{rz} and vertical displacement are zero.

(3) At the contact surface between the gasket and the anvil, a combined Coulomb friction and plastic friction model, which is described below, is utilized.

(4) Other surfaces not mentioned above are stress-free.

Finite element algorithms for solution of the boundary-value problems are presented in Feng et al.[28]

Friction model

According to the combined Coulomb friction and plastic friction model, there is complete cohesion between the contact pairs unless the shear (friction) stress reaches the critical value:

$$\tau_{crit} = \min\left[\mu(\sigma_c)\sigma_c, \tau_y(p)\right]. \tag{2}$$

When friction stress reaches τ_{crit}, contact sliding occurs in the radial direction. The critical shear stress $\tau_{crit} = \mu(\sigma_c)\sigma_c$ is related to the Coulomb friction, where μ is the friction coefficient and σ_c is the normal contact stress. However, the Coulomb friction stress cannot exceed the yield strength in shear $\tau_y(p)$, which is defined in terms of the yield strength under compression, σ_y, by $\tau_y = \sigma_y/\sqrt{3}$, based on the von Mises yield criterion. Thus, plastic sliding occurs when the Coulomb friction exceeds $\tau_y(p)$. In fact, it represents plastic shear flow within a very thin material layer immediately bellow the contact surface.

In this study the yield strength and the friction coefficient are assumed to be pressure and contact pressure dependent, respectively.

We assume $\mu = \mu_0 + c\sigma_c$ with two material parameters, which after calibration, looks like

$$\mu = 0.05 + 0.001\sigma_c, \quad \sigma_c \leq 37\,GPa. \tag{3}$$

Limitations on the contact stress exist because in FEM solutions, Coulomb sliding does not occur for $\sigma_c > 37\,GPa$, even for the highest maximum pressure of 380 GPa.

Elastoplastic material model under large strains and high pressure

We designate single and double contractions of the second-order tensors $\boldsymbol{A} = \{A_{ij}\}$ and $\boldsymbol{B} = \{B_{ij}\}$ over one and two indices as $\boldsymbol{A} \cdot \boldsymbol{B} = \{A_{ij}B_{jk}\}$ and $\boldsymbol{A} : \boldsymbol{B} = \{A_{ij}B_{ji}\}$, respectively. The subscript 's' denotes symmetrization, and the subscripts 'e' and 'p' denote elastic and plastic part of a tensor, respectively. The superscripts -1 and 'T' designate the inverse and transposition of a tensor. $\boldsymbol{I}$ is the second-order unit tensor.

The complete system of equations for a large elastoplastic deformation of a sample is as follows:[25,28]

Decomposition of the deformation gradient $\boldsymbol{F}$ in to elastic $\boldsymbol{F}_e$ and plastic $\boldsymbol{F}_p$ parts

$$\boldsymbol{F} = \partial\boldsymbol{r}/\partial\boldsymbol{r}_0 = \boldsymbol{F}_e \cdot \boldsymbol{F}_p = \boldsymbol{V}_e \cdot \boldsymbol{R}_e \cdot \boldsymbol{U}_p = \boldsymbol{V}_e \cdot \boldsymbol{V}_p \cdot \boldsymbol{R}_e, \tag{4}$$

where $\boldsymbol{r}$ and $\boldsymbol{r}_0$ are the position vectors of material points in the actual (deformed) configuration and the reference (undeformed) configuration, respectively; $\boldsymbol{V}_e$ and $\boldsymbol{V}_p$ are symmetric elastic and plastic left stretch tensors, respectively, $\boldsymbol{U}_p$ is the plastic right stretch tensor, and $\boldsymbol{R}_e$ is the proper orthogonal elastic rotation tensor.

Elastic strain $\boldsymbol{B}_e$ and its Jaumann objective time derivative

$$\boldsymbol{B}_e = 0.5\left(\boldsymbol{F}_e \cdot \boldsymbol{F}_e^T - \boldsymbol{I}\right), \quad \overset{\nabla}{\boldsymbol{B}_e} = \dot{\boldsymbol{B}}_e - 2(\boldsymbol{W} \cdot \boldsymbol{B}_e)_s. \tag{5}$$

Plastic strain (plotted in Figs 5–8)

$$\boldsymbol{\varepsilon}_p = \frac{1}{2}\boldsymbol{R}\cdot(\boldsymbol{U}_p\cdot\boldsymbol{U}_p - \boldsymbol{I})\cdot\boldsymbol{R}^T, \tag{6}$$

Decomposition of the velocity gradient $\boldsymbol{l}$, into symmetric deformation rate $\boldsymbol{d}$ and skew symmetric spin $\boldsymbol{w}$

$$\boldsymbol{l} = \boldsymbol{w}+\boldsymbol{d}, \quad \boldsymbol{d} = \overset{\triangledown}{\boldsymbol{B}}_e - 2(\boldsymbol{d}\cdot\boldsymbol{B}_e)_s + \boldsymbol{V}_e\cdot\boldsymbol{D}_p\cdot\boldsymbol{V}_e, \quad \boldsymbol{D}_p = \boldsymbol{R}_e\cdot(\dot{\boldsymbol{U}}_p\cdot\boldsymbol{U}_p^{-1})_s\cdot\boldsymbol{R}_e^T, \tag{7}$$

where D_p is the plastic deformation rate.

Isotropic elasticity rule

$$\boldsymbol{\sigma} = J^{-1}(2\boldsymbol{B}_e+\boldsymbol{I})\cdot\frac{\partial\Psi}{\partial\boldsymbol{B}_e}. \tag{8}$$

Here $\boldsymbol{\sigma}$ is the true Cauchy stress, $J = \mathrm{def}\,\boldsymbol{F}$ is the Jacobian, and Ψ is the specific Helmholtz free energy per unit undeformed volume.

Pressure-dependent yield surface (surface of perfect plasticity)

$$\varphi = \sqrt{(3/2)\boldsymbol{s}:\boldsymbol{s}} - \sigma_y(p) = 0, \tag{9}$$

where $\boldsymbol{s}$ is the deviatoric part of Cauchy stress $\boldsymbol{\sigma}$, and σ_y is the yield strength in compression.

Plastic flow rule

$$\boldsymbol{D}_p = \lambda\boldsymbol{s}/\sqrt{\boldsymbol{s}:\boldsymbol{s}}, \tag{10}$$

where $\lambda \geq 0$ is a scalar determined from the consistency condition $\dot{\varphi} = 0$.

The rate of accumulated plastic strain (plotted in Figs 5–8)

$$\dot{q} = (2\boldsymbol{D}_p:\boldsymbol{D}_p/3)^{0.5} = \sqrt{2/3}\lambda, \tag{11}$$

Equilibrium condition

$$\nabla\cdot\boldsymbol{\sigma} = 0, \tag{12}$$

where $\nabla\cdot$ is the divergence operator in the deformed configuration.

The yield strength in compression

We assume $\sigma_y = \sigma_{0y} + ap$ with two material parameters, which, after calibration, results in

$$\sigma_y = 1.8 + 0.1p; \quad p \leq 225\,\mathrm{GPa}. \tag{13}$$

Limitation on the pressure exists because, in FEM solutions, plastic flow does not occur for $p > 225$ GPa, despite the maximum pressure of 380 GPa.

Nonlinear isotropic elasticity for sample

The third-order nonlinear elastic Murnaghan potential is used:

$$\Psi(\boldsymbol{B}_e) = \frac{\lambda+2G}{2}I_1^2 - 2GI_2 + \frac{l+2m}{3}I_1^3 - 2mI_1I_2 + nI_3, \tag{14}$$

where λ, G, l, m, n are material parameters and I_1, I_2, I_3 are invariants of the elastic strain tensor:

$$I_1 = trace(\boldsymbol{B}_e), \quad I_2 = B_{e22}B_{e33} - B_{e23}^2 + B_{e11}B_{e33} - B_{e13}^2 + B_{e22}B_{e11} - B_{e12}^2, \quad I_3 = \det\boldsymbol{B}_e. \tag{15}$$

Furthermore, we have:

$$\frac{\partial I_1}{\partial\boldsymbol{B}_e} = \boldsymbol{I}, \quad \frac{\partial I_2}{\partial\boldsymbol{B}_e} = -\boldsymbol{B}_e + I_1\boldsymbol{I},$$

$$\frac{\partial I_3}{\partial\boldsymbol{B}_e} = \begin{bmatrix} B_{e22}B_{e33} - B_{e23}B_{e32} & B_{e23}B_{e31} - B_{e33}B_{e21} & B_{e21}B_{e32} - B_{e22}B_{e31} \\ B_{e23}B_{e31} - B_{e33}B_{e21} & B_{e11}B_{e33} - B_{e13}B_{e31} & B_{e12}B_{e31} - B_{e11}B_{e32} \\ B_{e21}B_{e32} - B_{e22}B_{e31} & B_{e12}B_{e31} - B_{e11}B_{e32} & B_{e11}B_{e22} - B_{e12}B_{e21} \end{bmatrix}. \tag{16}$$

Therefore, according to the elasticity rule Eq. (8), the Cauchy stress can be determined as:

$$\boldsymbol{\sigma} = J^{-1}(2\boldsymbol{B}_e+\boldsymbol{I})\cdot\left[\lambda I_1\boldsymbol{I} + 2G\boldsymbol{B}_e + lI_1^2\boldsymbol{I} + 2mI_1\boldsymbol{B}_e - 2mI_2\boldsymbol{I} + n\frac{\partial I_3}{\partial\boldsymbol{B}_e}\right] \tag{17}$$

Nonlinear anisotropic elasticity for diamond

To study the finite elastic strains in diamond, a free energy which includes the fourth-order terms of the Lagrangian strains $\boldsymbol{E}_e = 0.5(\boldsymbol{F}_e^T\cdot\boldsymbol{F}_e - \boldsymbol{I})$ is

utilized as:[41]

$$\begin{aligned}\Psi = {}&\tfrac{1}{2}C_{11}(\eta_1^2+\eta_2^2+\eta_3^2) + C_{12}(\eta_1\eta_2+\eta_2\eta_3+\eta_1\eta_3) + \tfrac{1}{2}C_{44}(\eta_4^2+\eta_5^2+\eta_6^2) \\ &+ \tfrac{1}{6}C_{111}(\eta_1^3+\eta_2^3+\eta_3^3) + \tfrac{1}{2}C_{112}[\eta_1^2(\eta_2+\eta_3)+\eta_2^2(\eta_1+\eta_3)+\eta_3^2(\eta_1+\eta_2)] \\ &+ C_{123}\eta_1\eta_2\eta_3 + C_{456}\eta_4\eta_5\eta_6 + \tfrac{1}{2}C_{144}(\eta_1\eta_4^2+\eta_2\eta_5^2+\eta_3\eta_6^2) \\ &+ \tfrac{1}{2}C_{155}[\eta_4^2(\eta_2+\eta_3)+\eta_5^2(\eta_1+\eta_3)+\eta_6^2(\eta_1+\eta_2)] \\ &+ \tfrac{1}{24}C_{1111}(\eta_1^4+\eta_2^4+\eta_3^4) + \tfrac{1}{6}C_{1112}[\eta_1^3(\eta_2+\eta_3)+\eta_2^3(\eta_1+\eta_3)+\eta_3^3(\eta_1+\eta_2)] \\ &+ \tfrac{1}{4}C_{1122}(\eta_1^2\eta_4^2+\eta_2^2\eta_5^2+\eta_3^2\eta_6^2) + C_{1123}\eta_1\eta_2\eta_3(\eta_1+\eta_2+\eta_3) \\ &+ \tfrac{1}{4}C_{1155}[\eta_1^2(\eta_6^2+\eta_5^2)+\eta_2^2(\eta_6^2+\eta_4^2)+\eta_3^2(\eta_5^2+\eta_4^2)] \\ &+ \tfrac{1}{2}C_{1255}[\eta_1\eta_2(\eta_4^2+\eta_5^2)+\eta_3\eta_2(\eta_6^2+\eta_5^2)+\eta_1\eta_3(\eta_6^2+\eta_4^2)] \\ &+ \tfrac{1}{2}C_{1266}(\eta_1\eta_2\eta_6^2+\eta_2\eta_3\eta_4^2+\eta_1\eta_3\eta_5^2) + C_{1456}\eta_4\eta_5\eta_6(\eta_1+\eta_2+\eta_3) \\ &+ \tfrac{1}{24}C_{4444}(\eta_4^4+\eta_5^4+\eta_6^4) + \tfrac{1}{4}C_{4455}(\eta_4^2\eta_5^2+\eta_6^2\eta_5^2+\eta_4^2\eta_6^2), \end{aligned} \tag{18}$$

where

$$\eta_1 = E_{e11}, \quad \eta_2 = E_{e22}, \quad \eta_3 = E_{e33}, \quad \eta_4 = 2E_{e23}, \quad \eta_5 = 2E_{e31}, \quad \eta_6 = 2E_{e12}. \tag{19}$$

Therefore, based on the elasticity law, the Cauchy stress in the diamond can be determined as:

$$\boldsymbol{\sigma} = \frac{1}{J}\boldsymbol{F}_e\cdot\frac{\partial\psi}{\partial\boldsymbol{E}_e}\cdot\boldsymbol{F}_e^T. \tag{20}$$

Material properties

Diamond. All elastic material constants are taken from Telichko et al.,[42] which, to the authors' knowledge, is the only reference that provides all third- and fourth-order elastic constants for diamond. These were determined using first principle simulations. Thus, we used the following elastic constants in our simulations:

$$\begin{aligned} C_{11} &= 1081.9, C_{12} = 125.2, C_{44} = 578.6, \\ C_{111} &= -7611, C_{112} = -1637, C_{123} = 640, C_{144} = -199, C_{166} = -4000, C_{456} = -1148, \\ C_{1111} &= 26,687, C_{1112} = 31,214, C_{1122} = 20,044, C_{1123} = -425, C_{1144} = -1385, C_{1155} = 10,741, \\ C_{1255} &= -264, C_{1266} = 819, C_{1456} = 487, C_{4444} = 11,328, C_{4455} = 528\,\mathrm{GPa}. \end{aligned} \tag{21}$$

Since available data for the third-order elastic constants from different references have significant scatter,[43–46] we assume that some of the fourth-order elastic constants are not precise either. Indeed, for the elastic constants from Telichko et al.,[42] we were unable to obtain the experimental equation of state collected in Maezono et al.[47] Thus, we changed C_{1112}, C_{1122}, and C_{1266} to the values indicated in Eq. (21) in order to receive good correspondence with the equation of state from Sato et al.[48]; see Fig. 12, and sample profile at highest pressure, see Fig. 2c.

A majority of equations of state of diamond determined by different methods[49,50] falls in between those from Sato et al.[48] and McSkimin and Andreatch.[51] Modifying the higher-order elastic properties of the diamond is another advancement over ref. [27].
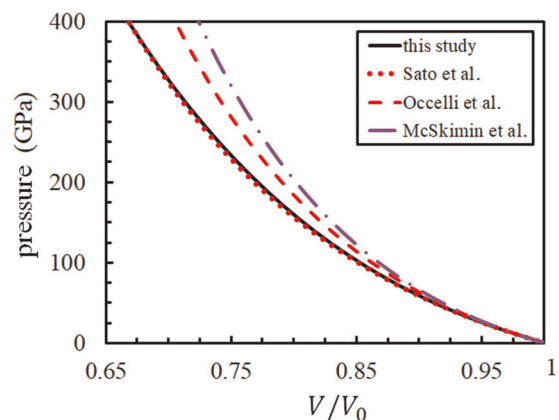

Fig. 12 Comparison of the equation of state for diamond from refs [48,51,53] and with current data based on Eq. (18) with elastic constants from Eq. (21)
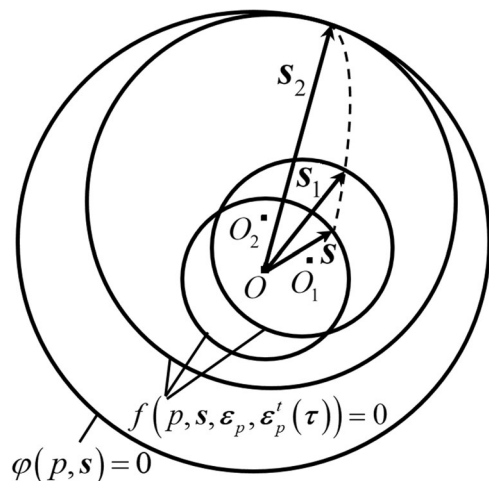
$$f\left(p, \boldsymbol{s}, \varepsilon_p, \varepsilon_p'(\tau)\right) = 0$$

$$\varphi(p, \boldsymbol{s}) = 0$$

Fig. 13 Schematic of evolution of the yield surface $f(p, \boldsymbol{s}, \varepsilon_p, \varepsilon_p^t(\tau)) = 0$ until it reaches the fixed surface of perfect plasticity $\varphi(p, \boldsymbol{s}) = 0$ in a "five-dimensional" space of deviatoric stresses $\boldsymbol{s}$ at fixed pressure p. The initial yield surface and the fixed surface of perfect plasticity $\varphi(p, \boldsymbol{s}) = 0$ are isotropic and pictured here as circles with their center at O. Two other yield surfaces depend on plastic strain $\boldsymbol{\varepsilon}_p$ at the current time t and the entire plastic strain history $\boldsymbol{\varepsilon}_p^t(\tau)$ before time t. These surfaces acquire strain-induced anisotropy, which is depicted by the shifted centers of the surfaces O_1 and O_2. However, when the yield surface reaches the fixed surface of perfect plasticity $\varphi(p, \boldsymbol{s}) = 0$, which is isotropic and plastic strain- and plastic strain history-independent, moves along it at further loading, the material deforms as perfectly plastic, isotropic with the fixed surface of perfect plasticity $\varphi(p, \boldsymbol{s}) = 0$

Tungsten. The elastic constants of the polycrystalline tungsten from Vekilov et al.[52] are used in this study, with some modifications:

$$\lambda = 206.5, \ G = 150.3, \ l = -404, \ m = -1{,}081, \ n = -1164\,\text{GPa}. \tag{22}$$

The third-order constants m and n for polycrystal have been found from the elastic constants for single crystal using the simplest Voight averaging scheme. Thus, they may have significant indeterminacy. We changed n and m to obtain a slightly better fit to the experimental pressure distribution curves for three lowest pressure.

Geometric interpretation of the postulate of perfect plasticity is presented in[24] and Fig. 13.

DATA AVAILABILITY

The authors declare that the main data supporting the findings of this study are available within the article. Extra data are available from the corresponding author upon request.

REFERENCES

1. Shen, G. & Mao, H. K. High-pressure studies with x-rays using diamond anvil cells. *Rep. Prog. Phys.* **80**, 016101 (2017).
2. Mao, H. K., Chen, X. J., Ding, Y., Li, B. & Wang, L. Solids, liquids, and gases under high pressure. *Rev. Mod. Phys.* **90**, 015007 (2018).
3. Dubrovinsky, L. et al. The most incompressible metal osmium at static pressures above 750 gigapascals. *Nature* **525**, 226–229 (2015).
4. Goettel, K. A., Mao, H. & Bell, P. M. Generation of static pressures above 2.5 megabars in a diamond-anvil pressure cell. *Rev. Sci. Instrum.* **56**, 1420–1427 (1985).
5. Hemley, R. J. et al. D. X-ray imaging of stress and strain of diamond, iron, and tungsten at megabar pressures. *Science* **276**, 1242–1245 (1997).
6. Li, B. et al. Diamond anvil cell behavior up to 4 mbar. *Proc. Natl Acad. Sci. USA* **115**, 1713–1717 (2018).
7. Jeanloz, R., Godwal, B. K. & Meade, C. Static strength and equation of state of rhenium at ultra-high pressures. *Nature* **349**, 687–689 (1991).
8. Wenk, H. R., Matthies, S., Hemley, R. J., Mao, H. K. & Shu, J. The plastic deformation of iron at pressures of the earth's inner core. *Nature* **405**, 1044–1047 (2000).
9. Deb, S. K., Wilding, M., Somayazulu, M. & McMillan, P. F. Pressure-induced amorphization and an amorphous-amorphous transition in densified porous silicon. *Nature* **414**, 528–530 (2001).
10. Mao, H. K. et al. Elasticity and rheology of iron above 220 GPa and the nature of the earth's inner core. *Nature* **396**, 741–743 (1998).
11. Dias, R. P. & Silvera, I. F. Observation of the Wigner-Huntington transition to metallic hydrogen. *Science* **355**, 715–718 (2017).
12. Ji, C. et al. Shear-induced phase transition of nanocrystalline hexagonal boron nitride to wurtzitic structure at room temperature and low pressure. *Proc. Natl. Acad. Sci. USA.* **109**, 19108–19112 (2012).
13. Meade, C. & Jeanloz, R. Effect of a coordination change on the strength of amorphous SiO2. *Science* **241**, 1072–1074 (1988).
14. Bridgman, P. W. Effects of high shearing stress combined with high hydrostatic pressure. *Phys. Rev.* **48**, 825–847 (1935).
15. Levitas, V. I. High-pressure mechanochemistry: conceptual multiscale theory and interpretation of experiments. *Phys. Rev. B* **70**, 184118 (2004).
16. Barge, N. V. & Boehler, R. Effect of non-hydrostaticity on the α-ε transition of iron. *High Press. Res.* **6**, 133–140 (2006).
17. Downs, R. & Singh, A. Analysis of deviatoric stress from nonhydrostatic pressure on a single crystal in a diamond anvil cell: the case of monoclinic aegirine, NaFeSi$_2$O$_6$. *J. Phys. Chem. Solids* **67**, 1995–2000 (2006).
18. Duffy, T. S. et al. Lattice strains in gold and rhenium under nonhydrostatic compression to 37 GPa. *Phys. Rev. B* **60**, 15063 (1999).
19. Merkel, S., Liermann, H. P., Miyagi, L. & Wenk, H. R. In situ radial x-ray diffraction study of texture and stress during phase transformations in bcc-, fcc- and hcp-iron up to 36 GPa and 1000 K. *Acta Mater.* **61**, 5144–5151 (2013).
20. Levitas, V. I. High pressure phase transformations revisited. *J. Physics: Condensed Matter* **30**, 163001 (2018).
21. Levitas, V. I. & Shvedov, L. K. Low pressure phase transformation from rhombohedral to cubic BN: experiment and theory. *Phys. Rev. B* **65**, 104109 (2002).
22. Blank, V. D. & Estrin, E. I. *Phase Transitions in Solids Under High Pressure.* (CRC Press, New York, 2014).
23. Moss, W. C., Hallquist, J. O., Reichlin, R., Goettel, K. A. & Martin, S. Finite-element analysis of the diamond anvil cell—achieving 4.6 Mbar. *Appl. Phys. Lett.* **48**, 1258–1260 (1986).
24. Levitas, V. I. *Large Deformation of Materials with Complex Rheological Properties at Normal and High Pressure* (Nova Science Publishers, New York, 1996).
25. Levitas, V. I., Polotnyak, S. B. & Idesman, A. V. Large elastoplastic strains and the stressed state of a deformable gasket in high pressure equipment with diamond anvils. *Strength Mater.* **3**, 221–227 (1996).
26. Merkel, S., Hemley, R. J. & Mao, H. K. Finite-element modeling of diamond deformation at multimegabar pressures. *Appl. Phys. Lett.* **74**, 656–658 (1999).
27. Feng, B., Levitas, V. I. & Hemley, R. J. Large elastoplasticity under static megabar pressures: formulation and application to compression of samples in diamond anvil cells. *Int. J. Plast.* **84**, 33–57 (2016).
28. Feng, B. & Levitas, V. I. Coupled elastoplasticity and plastic strain-induced phase transformation under high pressure and large strains: formulation and application to BN sample compressed in a diamond anvil cell. *Int. J. Plast.* **96**, 156–181 (2017).
29. Feng, B. & Levitas, V. I. Pressure self-focusing effect and novel methods for increasing the maximum pressure in traditional and rotational diamond anvil cells. *Sci. Rep.* **7**, 45461 (2017).
30. Lubliner, J. *Plasticity Theory* (Macmillan, New York, 1990).
31. Fleck, N. A., Muller, G. M., Ashby, M. F. & Hutchinson, J. W. Strain gradient plasticity—theory and experiment. *Acta Metall. Mater.* **42**, 475–487 (1994).
32. Chakravarthy, S. S. & Curtin, W. A. Stress-gradient plasticity. *Proc. Natl Acad. Sci. USA* **108**, 15716–15720 (2011).
33. Liu, D. B. & Dunstan, D. J. Material length scale of strain gradient plasticity: a physical interpretation. *Int. J. Plast.* **98**, 156–174 (2017).
34. Levitas, V. I., Ma, Y., Selvi, E., Wu, J. & Patten, J. High-density amorphous phase of silicon carbide obtained under large plastic shear and high pressure. *Phys. Rev. B* **85**, 054114 (2012).
35. Levitas, V. I. High-pressure phase transformations under severe plastic deformation by torsion in rotational anvils. *Mater. Trans.* **60**, 1294-1301 (2019).
36. Gao, Y. et al. Shear driven formation of nano-diamonds at sub-gigapascals and 300 K. *Carbon* **146**, 364–368 (2019).
37. Feng, B. & Levitas, V. I. Large elastoplastic deformation of a sample under compression and torsion in a rotational diamond anvil cell under megabar pressures. *Int. J. Plast.* **92**, 79–95 (2017).

38. Umeno, Y. & Černý, M. Effect of normal stress on the ideal shear strength in covalent crystals. *Phys. Rev. B* **77**, 100101 (2008).

39. Černý, M., Rehak, P., Umeno, Y. & Pokluda, J. Stability and strength of covalent crystals under uniaxial and triaxial loading from first principles. *J. Phys. Condens. Matter.* **25**, 035401 (2013).

40. Hsieh, S. et al. Imaging stress and magnetism at high pressures using a nanoscale quantum sensor. *Science*, resubmitted (2019); arXiv:1812.08796 [cond-mat.mes-hall; cond-mat.mtrl-sci], December 20, 2018, 68.

41. Vekilov, Y. K., Krasilnikov, O. M. & Lugovskoy, A. V. Elastic properties of solids at high pressure. *Physics-Uspekhi* **58**, 1106–1114 (2014).

42. Telichko, A. V. et al. Diamond's third-order elastic constants: ab initio calculations and experimental investigation. *J. Mater. Sci.* **52**, 3447–3456 (2017).

43. Hmiel, A., Winey, J. M., Gupta, Y. M. & Desjarlais, M. P. Nonlinear elastic response of strong solids: first-principles calculations of the third-order elastic constants of diamond. *Phys. Rev. B* **93**, 174113 (2016).

44. Winey, J. M., Hmiel, A. & Gupta, Y. M. Third-order elastic constants of diamond determined from experimental data. *J. Phys. Chem. Solids* **93**, 118–120 (2016).

45. Lang, J. M. & Gupta, Y. M. Experimental determination of third-order elastic constants of diamond. *Phys. Rev. Lett.* **106**, 125502 (2011).

46. Keating, P. N. Theory of the third order elastic constants of diamond-like crystals. *Phys. Rev.* **149**, 674–678 (1966).

47. Maezono, R., Ma, A., Towler, M. D. & Needs, R. J. Equation of state and raman frequency of diamond from quantum monte carlo simulations. *Phys. Rev. Lett.* **98**, 025701 (2007).

48. Sato, T., Ohashi, K., Sudoh, T., Haruna, K. & Maeta, H. The ambient-pressure lattice constants of pure diamond with natural isotopic composition are given as 3.566 88 Å at 300 K and 3.566 505 Å at 0 K. *Phys. Rev. B* **65**, 092102 (2002).

49. Holzapfel, W. B. Refinement of the ruby luminescence pressure scale. *J. Appl. Phys.* **93**, 1813–18 (2003).

50. Kunc, K., Loa, I. & Syassen, K. Equation of state and phonon frequency calculations of diamond at high pressures. *Phys. Rev. B* **68**, 094107 (2003).

51. McSkimin, H. J. & Andreatch, P. Elastic moduli of diamond as a function of pressure and temperature. *J. Appl. Phys.* **43**, 2944–48 (1972).

52. Vekilov, Y. K., Krasilnikov, O. M., Lugovskoy, A. V. & Lozovik, Y. E. Higher-order elastic constants and megabar pressure effects of bcc tungsten: ab initio calculations. *Phys. Rev. B* **94**, 104114 (2016).

53. Occelli, F., Loubeyre, P. & LeToullec, R. Properties of diamond under hydrostatic pressures up to 140 GPa. *Nat. Mater.* **2**, 151–154 (2003).

AUTHOR CONTRIBUTIONS

V.I.L. designed and supervised research, developed model, analyzed results and wrote paper. M.K. modified and extended the FEM algorithm, performed all simulations, and participated in analysis and writing paper. B.F. developed FEM algorithm and ABAQUS subroutines.

COMPETING INTERESTS

The authors declare no competing interests.

ADDITIONAL INFORMATION

Correspondence and requests for materials should be addressed to V.I.L.

Reprints and permission information is available at http://www.nature.com/reprints

Publisher's note Springer Nature remains neutral with regard to jurisdictional claims in published maps and institutional affiliations.